J Intell Robot Syst (2017) 87:43–57
DOI 10.1007/s10846-016-0452-y

Design and Analysis of a Novel 3D Decoupled Manipulator Based on Compliant Pantograph for Micromanipulation

Abdullah T. Elgammal · Mohamed Fanni · Abdelfatah M. Mohamed

Received: 23 February 2016 / Accepted: 1 December 2016 / Published online: 29 December 2016

Abstract A novel 3D compliant manipulator for micromanipulation is introduced based on pantograph linkage. The proposed manipulator provides decoupled 3DOF translational motions. The key design feature is the use of parallelograms, which maintain the orientation of the end-effector fixed. The proposed manipulator provides advantages over its counterparts in the literature. It has significantly higher workspace to size ratio if its pantograph acts as a magnification device. On the other hand, it has higher resolution if its pantograph acts as a miniaturizing device. This provides great flexibility in the design process to account for the limited variety of the micro-actuators and the large variety of the micro-scale tasks in terms of workspace and resolution. Thus, the proposed system possesses the characteristics of gearing (speed up or speed down). A suitable choice of flexure hinges and material is done. The position and velocity kinematic analysis are carried out. Analytical expressions are derived for singularity-free-workspace boundaries in terms of physical constraints of the flexure joints. Dexterity analysis is performed to evaluate the design performance. A synthesis methodology of the proposed manipulator is developed. A finite element analysis is carried out and a prototype is manufactured to validate the conceptual design. Simulation and experimental results have successfully demonstrated the linearity and consistency between input and output displacements with acceptable parasitic motions. Moreover, the manipulability of the proposed manipulator is found to be configuration independent. Also, the manipulator could have isotropic performance over its workspace for certain actuator setup.

Keywords Compliant parallel mechanism · 3D pantograph · Decoupled motions · Micromanipulation · Dexterity analysis · Workspace · Finite element analysis · Manipulator synthesis

A. T. Elgammal (✉) · M. Fanni · A. M. Mohamed
Department of Mechatronics and Robotics Engineering, Egypt-Japan University of Science and Technology (EJUST), P.O Box 179, New Borg El-Arab City, 21934, Alexandria, Egypt
e-mail: abdalla.gammal@ejust.edu.eg

M. Fanni
Mechanical Engineering Department, Mansoura University, Mansoura, Egypt
e-mail: mohamed.fanni@ejust.edu.eg

A. M. Mohamed
Department of Electrical Engineering, Assiut University, Assiut, 71516, Egypt
e-mail: abdelfatah.mohamed@ejust.edu.eg

1 Introduction

Micromanipulators are urgently required to manipulate minute objects for performing tasks as bio-cell manipulation, scanning tunneling microscope (STM), atomic force microscope (AFM), and part placement

in micro-assembly. These tasks demand high dexterity and precision that enable an unprecedented level of manipulability [1–3]. It is well known that parallel manipulators are widely popular and have intrinsic advantages over conventional serial manipulators as for the dynamic performance, rigidity, load carrying capacity, and accuracy [4, 5]. However, conventional parallel manipulators that use a rigid body mechanism suffer from certain disadvantages, such as the relatively small workspace and errors due to clearance, backlash, hysteresis, and frictions in the movable joints. Therefor it is a noteworthy challenge to obtain ultrahigh precision using mechanically assembled joints.

Compliant mechanisms are monolithic structures that provide the required motion from deflections by way of flexure hinges or flexible links inherent to the structure. The flexure hinges may be placed between relatively rigid members, referred henceforth to as links, to provide the desired motion of the mechanism, commonly determined by high precision actuators [6]. The compliant mechanism instead of traditional rigid body endows a mechanism with several merits including no backlash, free of friction and lubrication, vacuum compatibility, low cost and easy to fabricate [7]. Additionally, it can overcome the shortcomings existing in conventional precision systems with sliding and rolling bearings, and implement positioning with the capability of smooth motion [8–11]. The most common modeling methods of compliant mechanisms are finite element method, elliptic integral solution [12] and pseudo-rigid-body model (PRBM) [13]. The elliptic integral solution is frequently thought to be the most precise method however, it is viewed as a complex method [14] while, PRBM is considered as a straightforward method [15]. FEA modeling can be used to check the predictions of one of the previous modeling techniques as it provides a fine tune ability for the design towards the optimal performance [16].

Flexure hinge-based compliant mechanisms can be utilized into parallel manipulators for micropositioning applications however, most of compliant parallel mechanisms (CPM) have a coupled motion [17, 18]. Generally, a decoupled motion implies that each actuator delivers motion in one independent direction only. Typical pantograph manipulator is another sort of planar parallel manipulator that provides decoupled motions. It has several useful characteristics rather than kinematic decoupling as it provides a kinematic linearity between input and output motions. The development of a 2D compliant pantograph mechanism composed of large-deflective hinges has been proposed in [19]. A 2D compliant pantograph manipulator with end-effector of fixed orientation is developed in [20] using flexure joints. A 3D CPM has been proposed for micro/nano-manipulation with three decoupled translational motions [1]. However, the workspace volume to installation volume ratio is low [21].

The aim of this paper is to introduce a novel design of spatial 3DOF compliant pantograph manipulator in simple and compact structure for micromanipulation. The workspace volume to installation volume of the proposed compliant manipulator is higher than those of beforehand reported designs. The proposed CPM not only has a fixed orientation of the end-effector but also possesses a decoupled translational motions in the three orthogonal axes X, Y and Z using three linear actuators. The relation between the input displacements of the actuators and the output displacements of the end-effector is linear. The proposed CPM has the ability to produce an identical, enlarged, or miniaturized motion although this study is mainly focused on motion magnification.

This paper is organized as follows. The description of the new CPM is presented in Section 2. The position and velocity analysis is proposed in Section 3. Section 4 introduces a dexterity analysis of the CPM. In Section 5, the singularity-free-workspace boundary is found and expressed in closed form. Manipulator synthesis and a comparison with 3-PRC manipulator are carried out in Sections 6 and 7. Simulation and experimental results are done to confirm the performance of the manipulator in Section 8. Finally, conclusions is drawn in Section 9.

2 Development of the 3D compliant Pantograph

The typical 2D pantograph mechanism contains one parallelogram so that the movements of the actuators and the extreme point of the output link are pure decoupled translational motions in x and y directions. A 2D pantograph manipulator having end-effector with fixed orientation is obtained by adding a guiding mechanism to the 2D pantograph mechanism which consists of two parallelograms.

The premier challenging problem of creating a 3D translational parallel manipulator based on pantograph linkage is how to add a linear motion in z-direction to the end-effector of the previous 2D pantograph manipulator.

This new motion should be caused solely by one additional actuator without changing the orientation of the end-effector. This can be achieved by duplicating the 2D pantograph manipulator as shown in Fig. 1. For the sake of clarity, the two pantographs are virtually separated in Fig. 1 where, the numbers indicate the coincidence points. These pantographs are connecting together by means of two parallelograms with vertical axes joints. The new parallelograms keep the orientation of the end-effector fixed during the movement along the z-direction. The new actuator that controls the translation along z-direction is located at the extreme left point of the manipulator above the actuator that controls the y-direction movement. The actuator of x-direction movement is located at the right of the other actuators as shown in Fig. 1. Although the application of Grübler formula results in negative value which refers to non-moving structure, the movement of the system is a result of unique geometry similar to other parallel manipulators such as Delta and Tsai manipulators. The unique geometry

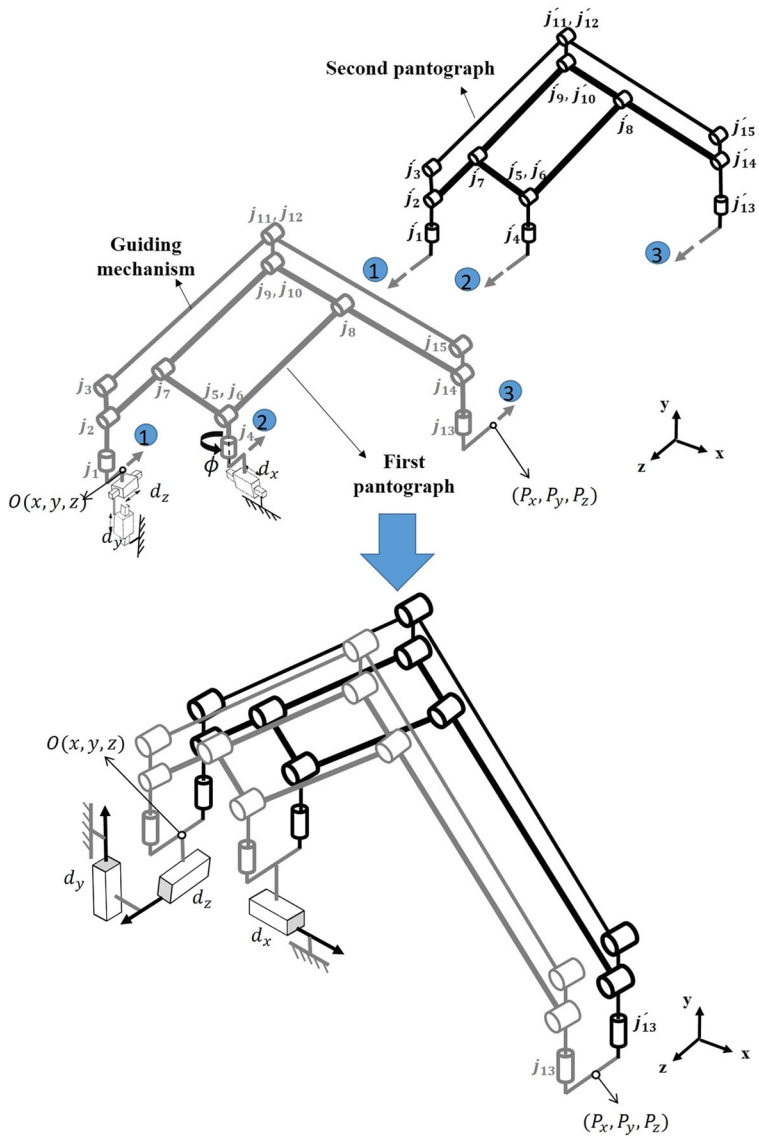

Fig. 1 Geometry of the proposed manipulator

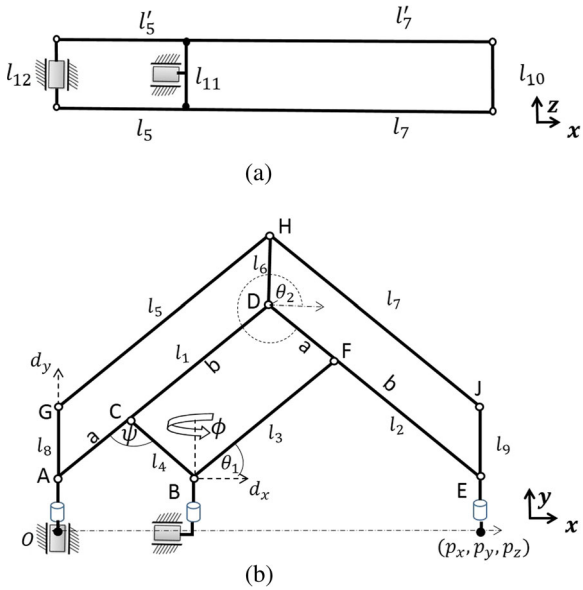

Fig. 2 Schematic drawing of the proposed manipulator **a** Top view, **b** Front view

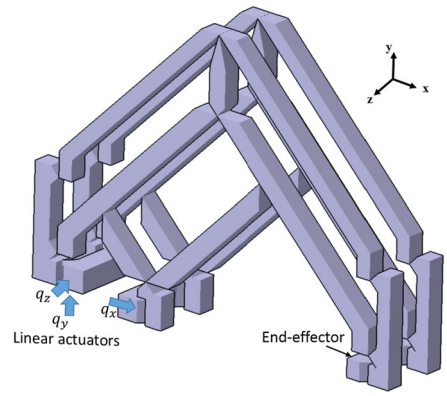

Fig. 4 The proposed compliant manipulator

here is that all the vertical axes of the joints are located in two parallel vertical planes. Figure 2 shows top and front views of the system.

The mobility of the manipulator can be calculated by geometrical approach of the basic movements as depicted in Fig. 3. The manipulator has 3DOF translational motions in x, y and z with a fixed orientation. The non-conventional structure of this interconnected parallel manipulator allows it to possess high workspace to size ratio comparable to that of serial manipulator. In Fig. 4, the 3D proposed compliant manipulator is designed by replacing each movable joint of the rigid body mechanism as shown in Fig. 1 with equivalent flexure joint. The design details of each flexure joint are illustrated in Fig. 5 which has different configuration depending on the initial position of the joint and how many links are connected together. The cantilevered notch hinges that reported in [19] has been used in the proposed design where, the thickness, length and width of the hinges are t, l and w respectively as shown in Fig. 6.

3 Kinematic Analysis

The mechanical system, shown in Fig. 2, has three input variables; two of them d_y and d_z are located at points **A** while the other one d_x at point **B**. The end-effector of the manipulator is link $l10$. According to Fig. 7, the following two vector-loop closure equations can be written as follows:

$$\overrightarrow{\mathbf{OE}} = \overrightarrow{\mathbf{OA}} + \overrightarrow{\mathbf{AD}} + \overrightarrow{\mathbf{DE}}, \tag{1}$$

$$\overrightarrow{\mathbf{OE}} = \overrightarrow{\mathbf{OB}} + \overrightarrow{\mathbf{BF}} + \overrightarrow{\mathbf{FE}}. \tag{2}$$

where O is the origin of the fixed coordinate system O-xyz. The axes x, y, and z coincide with the three

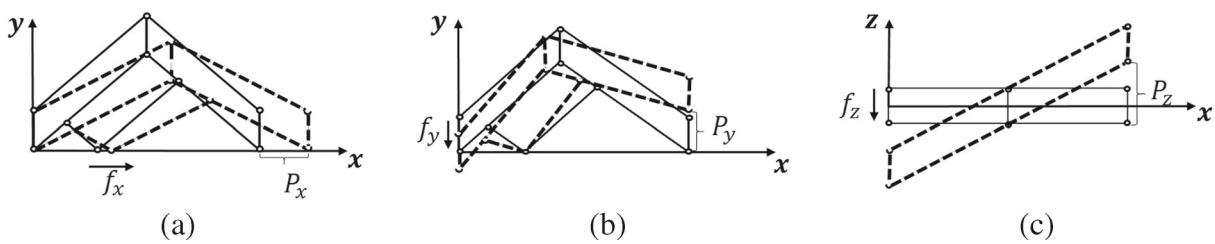

Fig. 3 The mobility analysis by geometrical approach

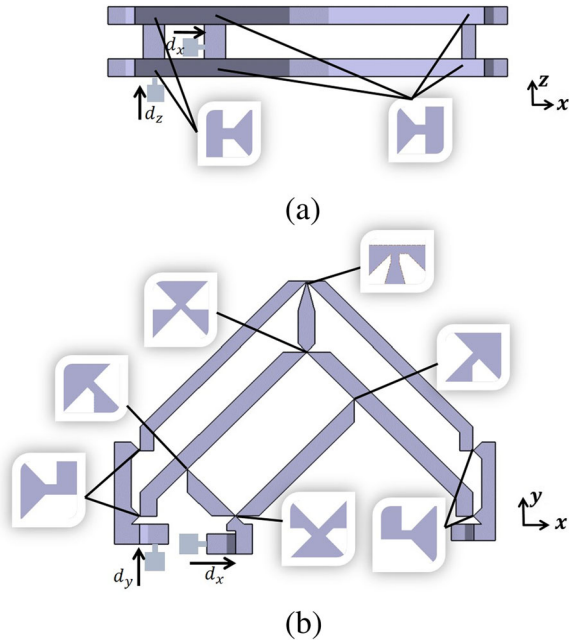

Fig. 5 Flexure hinges of the proposed compliant manipulator **a** Top view, **b** Front view

actuation axes. The position vector of the end-effector and the vector of the linear actuated joint variables are $p = [p_x, p_y, p_z]^T$ and $q = [d_x, d_y, d_z]^T$ respectively. Let $\overline{AC} = \overline{BC} = \overline{DF} = a$ and $\overline{CD} = \overline{BF} = \overline{FE} = b$. Loop equation (1) is used to obtain the following set constraint equations

$$p_x = (\cos\theta_1 + \cos\theta_2)(a+b)\cos\phi, \tag{3}$$

$$p_y - d_y = (\sin\theta_1 + \sin\theta_2)(a+b), \tag{4}$$

$$p_z - d_z = -(\cos\theta_1 + \cos\theta_2)(a+b)\sin\phi, \tag{5}$$

Similarly, three additional equations can be derived from loop (2)

$$p_x - d_x = (\cos\theta_1 + \cos\theta_2)b\cos\phi, \tag{6}$$

$$p_y = (\sin\theta_1 + \sin\theta_2)b, \tag{7}$$

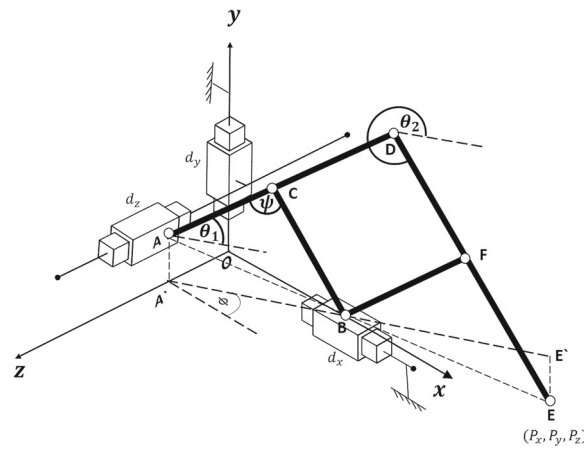

Fig. 7 Geometry of the main pantograph mechanism of the proposed manipulator

$$p_z = -(\cos\theta_1 + \cos\theta_2)b\sin\phi. \tag{8}$$

Dividing (3) by (6) to get the relation between the input actuator d_x and the output displacement p_x along X-axis

$$p_x = M_x d_x. \tag{9}$$

where $M_x = 1 + \frac{b}{a}$ is the magnification factor in x-direction. Similarly, from Eqs. 4 and 7 and from Eqs. 5 and 8, one gets the relationships between d_y and p_y and between d_z and p_z respectively.

$$p_y = -M_y d_y, \quad p_z = -M_z d_z. \tag{10}$$

where $M_y = M_z = \frac{b}{a}$ are the magnification factors in y- and z-direction respectively. The relations (9) and (10) illustrate the linearity between the input and output displacements as well as the decoupling of the translational motions. Differentiating (9) and (10) with respect to time, leads to the relationships between the linear velocities of input joint variables and those of the end-effector

$$\dot{p_x} = M_x \dot{d_x}, \quad \dot{p_y} = -M_y \dot{d_y}, \quad \dot{p_z} = -M_z \dot{d_z}. \tag{11}$$

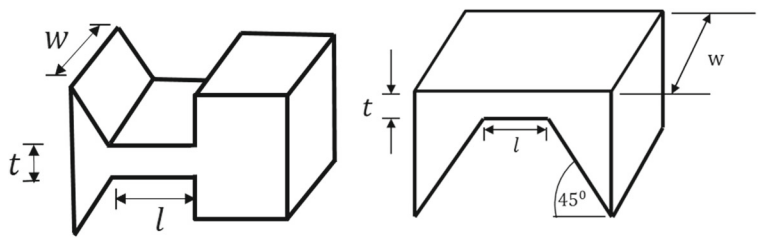

Fig. 6 Schematic of the flexure hinges

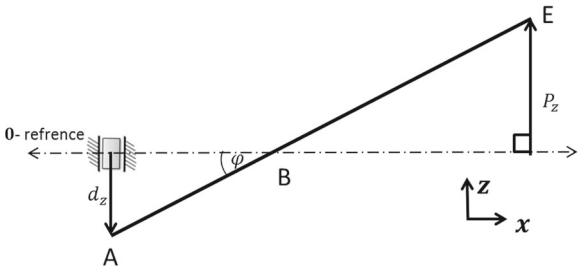

Fig. 8 Top view geometry for the 3D pantograph

Writing (11) in a matrix form leads to

$$\dot{p} = J\dot{q}. \tag{12}$$

where $\dot{p} = [\dot{p_x} \;\; \dot{p_y} \;\; \dot{p_z}]^T$ and $\dot{q} = [\dot{d_x} \;\; \dot{d_y} \;\; \dot{d_z}]^T$ are the vectors of the end-effector velocities and actuated joint rates respectively. J is the Jacobian of the 3D pantograph that can be written as

$$J = \begin{pmatrix} M_x & 0 & 0 \\ 0 & -M_y & 0 \\ 0 & 0 & -M_z \end{pmatrix} \tag{13}$$

4 Dexterity Analysis

Dexterity is regularly mentioned in the context of robotics research as an imperative issue for design, trajectory planning, and control. It has been developed as a measure for manipulator kinematic performance [22]. There are different indices of manipulator dexterity that introduced previously. Many of these indices were derived from the definition of manipulability proposed by Yoshikawa [23]. It can be expressed as

$$\omega = \sqrt{det(J J^T)} \tag{14}$$

For non redundant manipulators this expression reduces to

$$\omega = det(J) \tag{15}$$

Fig. 9 Workspace of the proposed manipulator at $a = 20mm$, $b = 50mm$, $\psi_{min} = \frac{\pi}{4}$, $\psi_{max} = \frac{3\pi}{4}$ and $\phi_{max} = \frac{\pi}{2}$

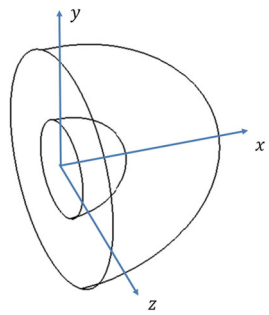

Fig. 10 Workspace of the proposed manipulator at $a = 20mm$, $b = 50mm$, $\psi_{min} = \frac{\pi}{4}$, $\psi_{max} = \frac{3\pi}{4}$ and $\phi_{max} = \frac{\pi}{4}$

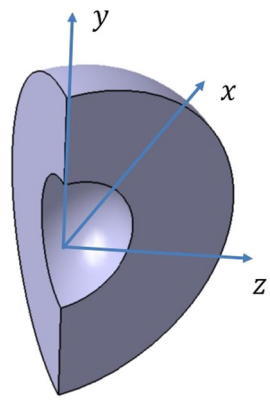

It can be noted that the Jacobian matrix in Eq. 13 for the proposed CPM depends only on links' lengths. Hence, The manipulability is configuration independent according to

$$\omega = \frac{b^2\ (a+b)}{a^3} \tag{16}$$

In order to achieve isotropic performance over the entire workspace, all actuators should acting on the same link, either $l11$ or $l12$ in Fig. 2.

5 Workspace Determination

The reachable workspace of the proposed 3-DOF pantograph is determined in this section taking into account the physical limits of its joints. Referring to Figs. 7 and 8

$$\overline{AB}^2 = 2a^2(1 - \cos\psi) = d_x^2 + d_y^2 + d_z^2 \tag{17}$$

The angle rotated by this system around y-axis can be calculated as

$$\tan\phi = \frac{d_z}{d_x}, \quad or \quad \tan\phi = \frac{M_x p_z}{-M_z p_x} \tag{18}$$

5.1 Workspace of The Proposed Manipulator as a Rigid Body Mechanism

The workspace can be calculated for the rotary angles $\psi = [0, \pi]$ and $\phi = [-\pi/2, \pi/2]$. Substituting maximum and minimum values of ψ and ϕ into Eqs. 17 and 18 and using Eqs. 9 and 10, the workspace boundary equation is found to be a semi-prolate-ellipsoid and

can be represented as

$$\frac{{p_x}^2}{(2aM_x)^2}+\frac{{p_y}^2}{(2aM_y)^2}+\frac{{p_z}^2}{(2aM_z)^2}=1,\quad p_x\geq 0 \quad (19)$$

where two of semi-axes are equal and less than the third one.

5.2 Workspace of The Proposed Compliant Manipulator Considering Rotary Limits of Flexure Hinges

Let the ranges of the rotary angles ψ and ϕ are $[\psi_{min},\psi_{max}]$ and $[-\phi_{max},\phi_{max}]$ respectively, where $0<\psi_{min}<\psi_{max}<\pi$ and $\phi_{max}<\frac{\pi}{2}$. Substituting the maximum and minimum values of ψ into Eq. 17, the range of each linear actuator can be found as

$$d_{xmax}=\sqrt{2a^2(1-\cos\psi_{max})},\quad d_{xmin}=0 \quad (20)$$

$$d_{y_{max,min}}=\pm\sqrt{2a^2(1-\cos\psi_{max})} \quad (21)$$

Similarly, substituting the maximum and minimum values of ψ and ϕ into Eqs. 17 and 18 to figure out the range of the third actuator $d_{z_{max,min}}$ as

$$d_{z_{max,min}}=\pm\sqrt{\frac{2a^2(1-\cos\psi_{max})}{1+\frac{1}{\tan^2\phi_{max}}}} \quad (22)$$

The limit values ψ_{max} and ψ_{min} are assigned Taking into consideration the physical limitations of all joints having horizontal axes. Similarly, the limit value ϕ_{max} is assigned taking into consideration all joints having vertical axes. It should be noted from Eq. 17 that the workspace is the bounded volume by two semi-ellipsoid at ψ_{max} and ψ_{min} as shown in Fig. 9. The first boundary equation is given by

$$\frac{{p_x}^2}{(M_x)^2}+\frac{{p_y}^2}{(M_y)^2}+\frac{{p_z}^2}{(M_z)^2}=2a^2(1-\cos\psi_{max}),\quad p_x\geq 0 \quad (23)$$

and the other one is

$$\frac{{p_x}^2}{(M_x)^2}+\frac{{p_y}^2}{(M_y)^2}+\frac{{p_z}^2}{(M_z)^2}=2a^2(1-\cos\psi_{min}),\quad p_x\geq 0 \quad (24)$$

The above workspace is calculated regardless of limitations of the angle ϕ. Use Eq. 18 to take the limitations of ϕ into consideration. Two vertical planes containing y-axis at angle $\pm\phi_{max}$ with respect to x-axis is cutting off two parts of the previous workspace as shown in Fig. 10. Another factor that affects the workspace volume are the singularities due to aligning of the main pantograph links with the guiding mechanism links which occur when $\theta_1=\pm\frac{\pi}{2}$ or $\theta_2=\pm\frac{\pi}{2}$. Referring to Fig. 7, the boundary of these singularities can be determined using the following vector-loop equation

$$\vec{\mathbf{OB}}=\vec{\mathbf{OA'}}+\vec{\mathbf{A'A}}+\vec{\mathbf{AC}}+\vec{\mathbf{CB}}, \quad (25)$$

hence, the scalar equations are given as

$$d_x-a\cos\theta_1\cos\phi=-a\cos\theta_2\cos\phi \quad (26)$$

$$d_y+a\sin\theta_1=a\sin\theta_2 \quad (27)$$

$$d_z-a\cos\theta_1\sin\phi=-a\cos\theta_2\sin\phi \quad (28)$$

Substitute the singular values of θ_1 into Eqs. 26, 27 and 28 with Squaring and summing each side of equations to eliminate ϕ and θ_2, this produces two equal semi-ellipsoids at different centers as following

$$\frac{{p_x}^2}{(aM_x)^2}+\frac{(p_y\pm aM_y)^2}{(aM_y)^2}+\frac{{p_z}^2}{(aM_z)^2}=1,\quad p_x\geq 0 \quad (29)$$

Similarly, substituting singular values of θ_2 gives two identical semi-ellipsoids as in Eq. 29. The reachable workspace of the proposed manipulator after removing these singularities is shown in Fig. 11. Note that ψ and ϕ are related to the angular deflection of the flexure joint δ which is related to the stress σ [17] as

$$\delta=\frac{0.148l}{Et}\sigma \quad (30)$$

where E, l and t are modulus of elasticity, length and thickness of the flexure joint respectively as shown

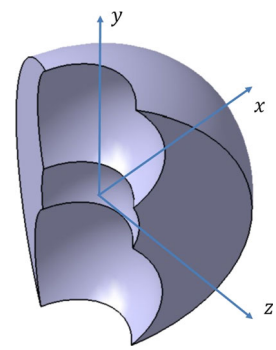

Fig. 11 Reachable workspace of the proposed manipulator at $a=20mm$, $b=50mm$, $\psi_{min}=\frac{\pi}{4}$, $\psi_{max}=\frac{3\pi}{4}$ and $\phi_{max}=\frac{\pi}{4}$

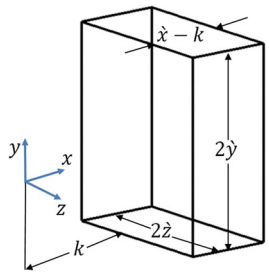

Fig. 12 Maximum usable cuboid workspace

in Fig. 6. The maximum joint angles ψ_{max}, ψ_{min} and ϕ_{max} are determined using the above formula at allowable stress σ_{all}

$$\psi_{max} = \frac{\pi}{2} + \frac{0.148l}{Et}\sigma_{all} \tag{31a}$$

$$\psi_{min} = \frac{\pi}{2} - \frac{0.148l}{Et}\sigma_{all} \tag{31b}$$

$$\phi_{max} = \frac{0.148l}{Et}\sigma_{all} \tag{31c}$$

It is assumed that all flexure joints have the same dimensions.

The desired and usable workspace for translational micromanipulators is defined as a maximum cuboid inscribed within the reachable workspace as defined in Figs. 12 and 13. Maximization of this rectangular box volume is an optimization problem that will be solved by Sequential quadratic programming (SQP). The objective function is the cuboid volume v which can be formalized according to:

$$v = 4(\dot{x} - k)\dot{y}\,\dot{z} \tag{32}$$

where $\dot{x}$, $\dot{y}$ and $\dot{z}$ are the design variables as shown in Fig. 12 and $k = \max(aM_x, a\sqrt{2M_x^2(1-\cos\psi_{min})})$ is the largest semi-major axis of inner ellipsoids in Eqs. 24 and 29. The objective function has to be maximized under the constraints

$$\frac{\dot{x}^2}{(M_x)^2} + \frac{\dot{y}^2}{(M_y)^2} + \frac{\dot{z}^2}{(M_z)^2} \le 2a^2(1-\cos\psi_{max}) \tag{33a}$$

$$\frac{k^2}{(M_x)^2} + \frac{\dot{y}^2}{(M_y)^2} + \frac{\dot{z}^2}{(M_z)^2} \le 2a^2(1-\cos\psi_{max}) \tag{33b}$$

where, the lower and upper limits of the design variables are

$$k \le \dot{x} \le a\sqrt{2M_x^2(1-\cos\psi_{max})}, \tag{34a}$$

$$0 \le \dot{y} \le a\sqrt{2M_y^2(1-\cos\psi_{max})}, \tag{34b}$$

$$0 \le \dot{z} \le \min\left(\frac{aM_z\dot{x}\tan\phi_{max}}{M_x}, a\sqrt{2M_z^2(1-\cos\psi_{max})}\right) \tag{34c}$$

The optimization is done using SQP toolbox in MATLAB at $a = 20mm$, $b = 50mm$, $t = 0.1mm$, and $l = 5mm$ and assuming the manipulator is made of polypropylene with Young's modulus of $2\,GPa$ and $\sigma_{all} = 23.5\,MPa$. Substituting in Eq. 31 to figure out the maximum angles deflection $\psi_{min} = 1.49\,rad$, $\psi_{max} = 1.65\,rad$ and $\phi_{max} = 0.0795\,rad$. The maximum volume is found to be $1.78 \times 10^{-6}\,m^3$ and the optimum design variables are: 0.1001, 0.0163 and 0.0054 for $\dot{x}$, $\dot{y}$ and $\dot{z}$ respectively. Figure 14 shows the usable cuboid workspace of the proposed manipulator.

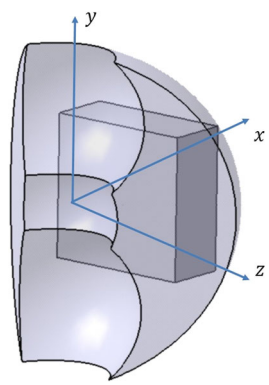

Fig. 13 Maximum cuboid inscribed within the reachable workspace assuming $a = 20mm$, $b = 50mm$, $\psi_{min} = \frac{\pi}{4}$, $\psi_{max} = \frac{3\pi}{4}$ and $\phi_{max} = \frac{\pi}{4}$

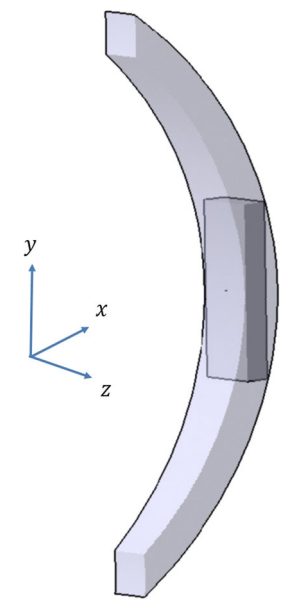

Fig. 14 Maximum cuboid inscribed within the reachable workspace at $a = 20mm$, $b = 50mm$, $t = 0.1mm$ and $l = 5mm$

Table 1 Physical constraints

Physical constraint	Proposed manipulator	3-PRC manipulator
Physical size	$2.107 \times 10^{-3} m^3$	
Actuators stroke	$140\mu m \times 140\mu m \times 140\mu m$	
Joint type	Circular notch joint	
Joint Dimensions	$t = 1mm$, $r = 1mm$, $w = 3mm$ and $h = 3mm$	
Material	Titanium alloy Ti-6Al-4V	
Properties	Young's Modulus Yield strength Poisson's ratio	
	$E = 113.8GPa$ $\sigma_y = 880MPa$ 0.342	
Workspace	$2.22 \times 10^{-9} m^3$, $\frac{b}{a} = 9$	$2.74 \times 10^{-12} m^3$
(cuboid)	$4.11 \times 10^{-10} m^3$, $\frac{b}{a} = 5$	
Ratio	1.05×10^{-6} at $\frac{b}{a} = 9$	1.3×10^{-9}
	1.95×10^{-7} at $\frac{b}{a} = 5$	

6 Manipulator Synthesis

The aim of the synthesis problem is to find the minimum dimensions of the proposed manipulator made of certain material to be able to generate a prespecified usable cuboid workspace. Given a certain material and required workspace as a cuboid with dimensions d_1, d_2 and d_3, the design variables are links' lengths a and b and dimensions of flexure joints l and t in addition to the parameters of the maximum usable workspace $\grave{x}$, $\grave{y}$ and $\grave{z}$. The optimum design problem can be formulated as follows

$$\min_{D.V} . \quad f = w_1 \frac{a}{a_{nom}} + w_2 \frac{b}{b_{nom}} + w_3 \frac{nl}{l_{nom}} + w_4 \frac{nt}{t_{nom}} \tag{35}$$

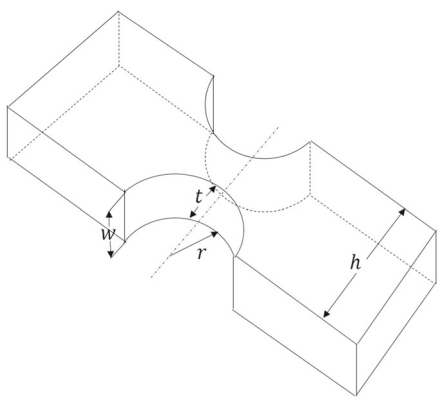

Fig. 15 Schematic of the circular notch joint

subjected to constraints (33) and (34) in addition to

$$\min(\grave{x} - k, 2\grave{y}, 2\grave{z}) \geq \min_{i=1,2,3} d_i \tag{36a}$$

$$\max(\grave{x} - k, 2\grave{y}, 2\grave{z}) \geq \max_{i=1,2,3} d_i \tag{36b}$$

$$\text{median}(\grave{x} - k, 2\grave{y}, 2\grave{z}) \geq \underset{i=1,2,3}{\text{median}}\, d_i \tag{36c}$$

where $a_{nom} = 15\,mm$, $b_{nom} = 30\,mm$, $l_{nom} = 0.2\,mm$ and $t_{nom} = 0.1\,mm$ are nominal values of links and joint variables, while w_1, w_2, w_3 and w_4 are weighting constants with summation equal to 1 and $n = 30$ is a number of flexure joints. The above constraints are used to ensure that the prespecified workspace is enclosed within the usable workspace. Since all flexure joints have the same dimensions l and t, lead to $\psi_{min} = \pi - \psi_{max}$ and $\phi_{max} = \psi_{max} - \pi$ using Eq. 31. The prespecified workspace volume of the manipulator is $1mm^3$ where $d_1 = d_2 = d_3 = 1mm$ and the manipulator is made of polypropylene. SQP is used for solving the above nonlinear constrained optimization problem with $w_1 = w_2 = w_3 = w_4 = 0.25$. The design variables are found to be $a = 10mm$, $b = 56.948$, $t = 0.1mm$, $l = 0.666mm$, $x = 95.1768$, $y = 0.51$ and $z = 0.51$, where the maximum cuboid dimensions are $1mm$ x $1.03mm$ x $1.03mm$. The corresponding and required actuators stroke can be determined as $\delta_x = \frac{d_1}{M_x}$, $\delta_y = \frac{d_2}{M_y}$ and $\delta_z = \frac{d_3}{M_z}$ for x, y and z directions respectively. Actuators stroke may be taken into account in the optimization problem as additional constraints as follows

$$\frac{b+a}{a} \geq \frac{d}{\delta_x}, \quad \frac{b}{a} \geq \frac{d}{\delta_y} \tag{37}$$

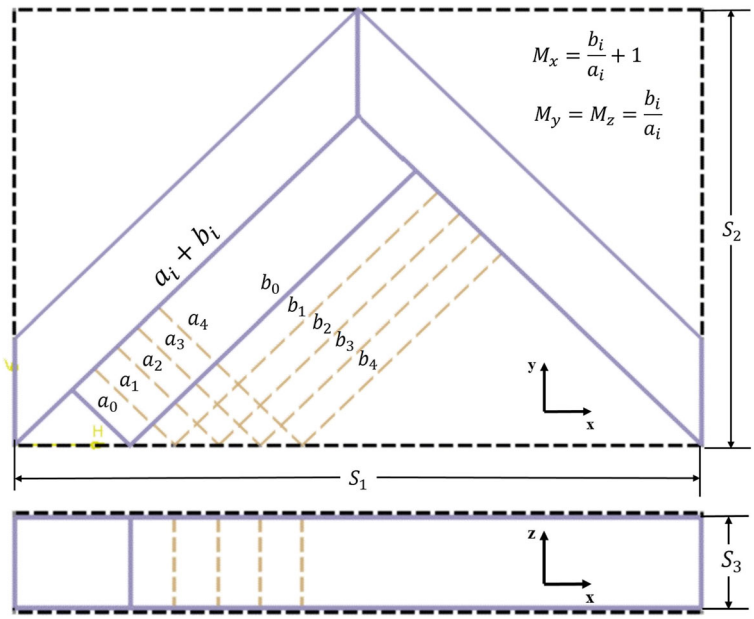

Fig. 16 The physical size of the proposed manipulator with different magnification factors

where δ_x, δ_y, δ_z and d are known and assuming that the prespecified workspace is a cube, where $d_1 = d_2 = d_3 = d$. Using the above constraints, one can specify the required magnification factors necessary to match the required workspace of certain task with the available actuators sizes.

7 Comparison between the Proposed Manipulator and the 3-PRC Manipulator

A ratio of workspace volume to physical size is calculated for the proposed manipulator and 3-PRC manipulator that has been proposed in [24]. The comparison is done under the same constraints of the physical size of each manipulator, actuators' strokes, material and flexure joint type and dimensions as shown in Table 1. It should be noted that the physical size of each manipulator is calculated as cuboid volume taking into account the size of actuators. PZT actuators are selected from Physik Instrumente (PI) as P-621.ZCD and two of P-6221CL for both manipulators. The flexure hinge type is a circular notch joint as shown in Fig. 15, where the maximum angular deflection δ_{max} is related to the allowable stress σ_{all} [17] as

$$\delta_{max} = \frac{3\pi}{4E}\sqrt{\frac{r}{t}}\sigma_{all} \tag{38}$$

where E, r and t are modulus of elasticity, radius and thickness of the circular notch joint respectively. The ratio of the proposed manipulator is equal to 150 times the ratio of the 3-PRC manipulator at $\frac{b}{a} = 5$. Moreover, this ratio could be increased or decreased without changing the physical size of the proposed manipulator by just varying the magnification factor, $\frac{b}{a}$, while the lenght, $a + b$, and hence the cuboid volume, $S_1 S_2 S_3$, have constant values as shown in Fig. 16. However, the magnification factor should not be very high to satisfy the precise motion based on the required spatial resolution and actuator resolution. The ratio $\frac{b}{a}$ could be also less than 1 to be used in a nanomanipulation with accurate motion,

Table 2 Workspace to size ratio of the proposed manipulator and 3PRC manipulator

Physical constraint	Proposed manipulator	3-PRC manipulator
Workspace (cuboid)	$2.74 \times 10^{-12} m^3$	
Actuators stroke	$140\mu m \times 140\mu m \times 140\mu m$	
Physical size	$2.64 \times 10^{-4} m^3$	$2.107 \times 10^{-3} m^3$
Ratio	1.04×10^{-8}	1.3×10^{-9}

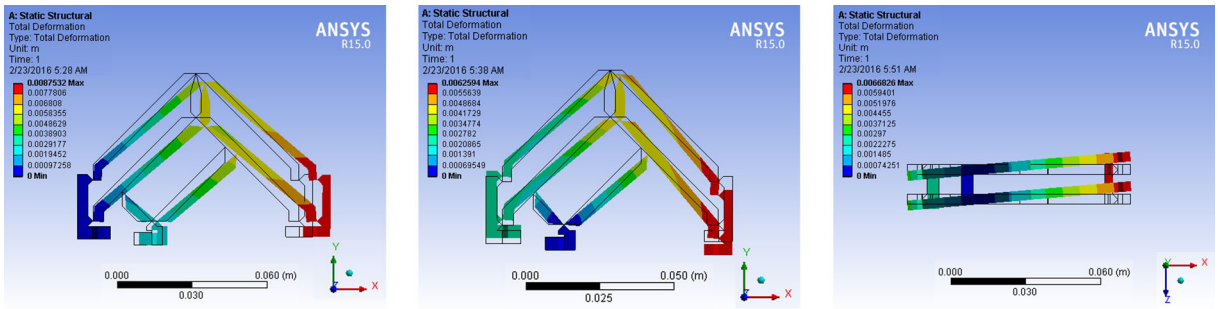

Fig. 17 Finite-element model

where the function of the proposed manipulator here is to increase the resolution rather than increasing the workspace.

Another comparison is carried out with different physical size of each manipulator, nevertheless constraints of material properties, actuators stroke and flexure joint are still identical as well as the usable workspace. This could be happened when the actuator in the x-direction is located at the same link of actuators y- and z-direction, where the magnification factors of all directions are equal $M_x = M_y = M_z = 1$ and $a = b \geq 11mm$. Therefore the results of this comparison is demonstrated in Table 2 and it shows that the ratio of the proposed manipulator is equal to 7.98 times of the ratio of the 3-PRC manipulator. The physical size of the manipulator will not be very small because of the actuators size although the links lengths' are very small. The magnification factor is chosen to be 1 to make the comparison of the workspace to size ratio between the two manipulators with the same workspace resolution.

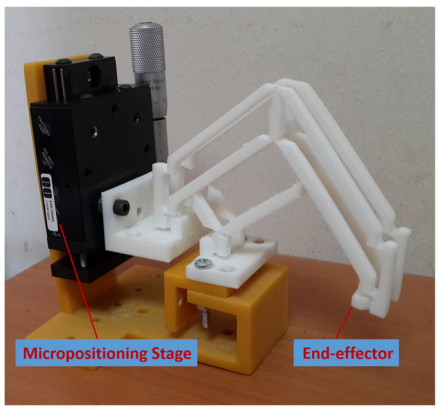

Fig. 18 The prototype of the proposed compliant manipulator

8 Simulation and Experimental Results

Position analysis of the proposed CPM is carried out using finite element method (FEM) via ANSYS® as shown in Fig. 17 to verify the conceptual design of the proposed manipulator. Figures 4 and 5 show the 3D compliant manipulator that has been built on CATIA® software. A prototype is manufactured using 3D printer and is depicted in Fig. 18. The experimental setup comprises a measuring microscope Mar-Vision MM320 and micropositioning stage as shown in Fig. 19. The proposed manipulator is made of Flexible-T material with $a = 20\,mm$, $b = 50\,mm$, $t = 0.8\,mm$, $l = 0.8\,mm$ and $w = 5\,mm$. The aim of the simulation and experimental data is to investigate the performance and to ensure that the parasitic displacements are very small to be suitable for micromanipulation, where the precision is inversely proportional to the parasitic motion. The flexure joints of the configuration corresponding to the middle of the input displacement ranges have zero deflection. As mentioned previously, M_x, M_y and M_z are the magnification factors and equal to 3.5, 2.5 and 2.5

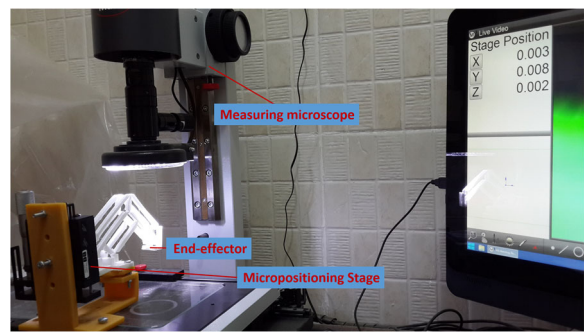

Fig. 19 Experimental setup

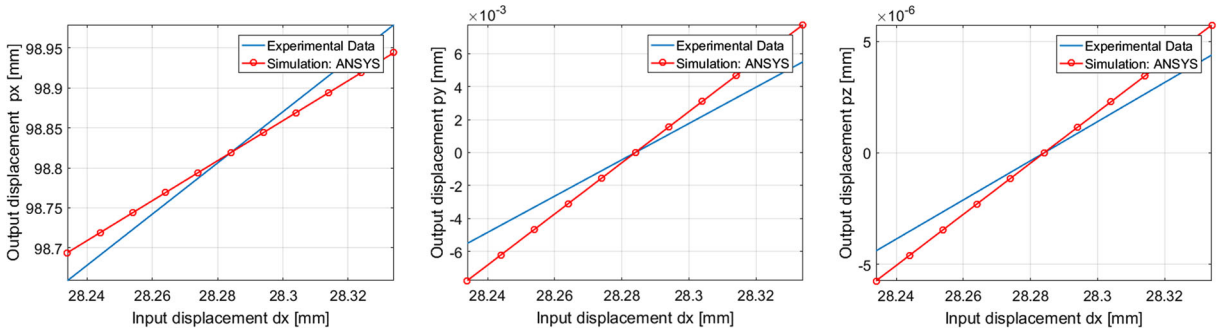

(a) Motion in **x**-axis (b) Motion in **y**-axis (c) Motion in **z**-axis

Fig. 20 Output displacements versus input displacement d_x

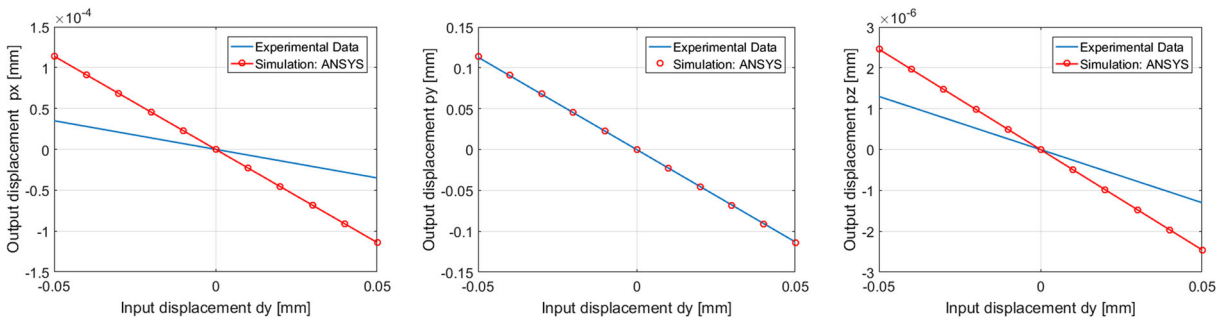

(a) Motion in **x**-axis (b) Motion in **y**-axis (c) Motion in **z**-axis

Fig. 21 Output displacements versus input displacement d_y

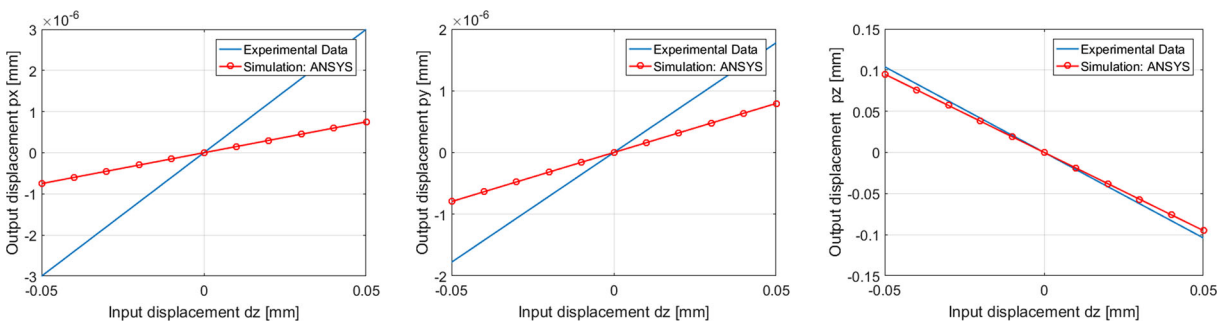

(a) Motion in **x**-axis (b) Motion in **y**-axis (c) Motion in **z**-axis

Fig. 22 Output displacements versus input displacement d_z

Table 3 The actual and ideal ratios of output to input displacements

Input Ratio	$\lvert\frac{p_x}{d_{in}}\rvert$ (|ideal ratio|)	$\lvert\frac{p_y}{d_{in}}\rvert$ (|ideal ratio|)	$\lvert\frac{p_z}{d_{in}}\rvert$ (|ideal ratio|)
d_x	3.2 (3.5)	0.11 (0)	0.88×10^{-4} (0)
d_y	0.0007 (0)	2.26 (2.5)	2.6×10^{-5} (0)
d_z	6×10^{-5} (0)	3.55×10^{-4} (0)	2.08 (2.5)

respectively according to Eqs. 9 and 10. However, these factors are considered as ideal values corresponding to rigid body mechanism. The input variables d_x, d_y and d_z range from $28.234\,mm$ to $28.334\,mm$, $-50\,\mu m$ to $50\,\mu m$ and $-50\,\mu m$ to $50\,\mu m$ respectively. Figure 20 shows the displacements of the end-effector in x-, y-, z-direction (p_x, p_y, p_z) as a result of the input displacements along x-axis (d_x) at point **B**. It shows that the output p_x is linear with magnification factor $\grave{M}_x = 3.2$ experimentally. The other parasitic motions are also linear and relatively small for p_y and inconsiderable for p_z as shown in Fig. 20a and b respectively. Figures 21 and 22 show the position of the end-effector (p_x, p_y, p_z) as a result of the input displacements along y-axis (d_y) and z-axis (d_z) respectively at point **A**. The amplification factors for y- and z-direction is found to be linear as $\grave{M}_y = 2.26$ and $\grave{M}_z = 2.08$ which illustrated in Figs. 21b and 22c respectively. Figures 21a, c, 22a and b show relatively small parasitic motions. The actual and ideal ratios of output displacements to input displacements are illustrated in Table 3. In contrast to the rigid body mechanism, the proposed CPM does not have pure decoupled motions and hence has small parasitic motions due to its inherent flexibility. Also, the magnification factors are not the same as the ideal ones due to the shifted rotation center of the flexure joints. It should be noted that the magnification factors not only depend on links lengths' but also are inversely proportional to the thickness, length and width of the flexure joints.

Similarly, the orientation of the end-effector is determined in simulation only at the same range for each input variable as can be seen in Fig. 23. In Fig. 23a, the orientation of the end-effector around x-and y-axis are zero and the maximum angle around z-axis is $\pm 0.0036^o$ when the input variable d_x is applied. The second input variable d_y is applied as shown in Fig. 23b. It shows zero rotation angles around x-and very small angles around y-axis and d z-axis. Figure 23c illustrates the orientation of the end-effector which is zero around both x- and z-axis and 0.06^o around y-axis as a maximum value resulting from input displacement d_z. These small errors of displacements and orientation of the end-effector indicate the kinematic decoupling performance of the proposed manipulator. The output displacements are all linear even in the undesirable motions which could be compensated using an appropriate controller. The maximum von-Mises stress is determined for the proposed CPM by FEM at maximum displacements as well as for each flexure joint at the same range of input variables d_x, d_y and d_z as shown in Fig. 24, where flexure joints $j_1, j_2, ..., j_{15}$ and $j'_1, j'_2, ..., j'_{15}$ are depicted in Fig. 1. Figure 24 shows that the maximum stress of each flexure hinge is much smaller than the yield strength of the material which equals $32MPa$. The reachable workspace and installation volume are determined experimentally of the proposed manipulator which equal $1.504 \times 10^{-11} m^3$ and $6.54 \times 10^{-4} m^3$ respectively. Although the actuators' strokes of the proposed manipulator, $100\mu m \times 100\mu m \times 100\mu m$, are less than those of the 3PRC manipulator, $140\mu m \times 140\mu m \times 140\mu m$, they give higher workspace. Furthermore, the workspace to size ratio of the proposed manipulator, 2.298×10^{-8}, equals 17 times the ratio of the 3PRC manipulator, 1.3×10^{-9}, where the workspace and installation volumes of the 3PRC manipulator are $2.74 \times 10^{-12} m^3$ and $2.107 \times 10^{-3} m^3$ respectively.

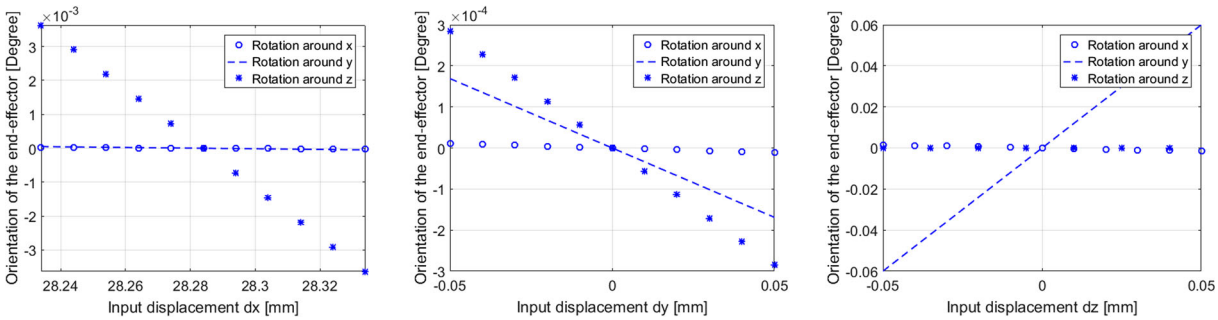

(a) Motion in **x**-axis (b) Motion in **y**-axis (c) Motion in **z**-axis

Fig. 23 Orientation of the end-effector versus input displacements d_x, d_y and d_z

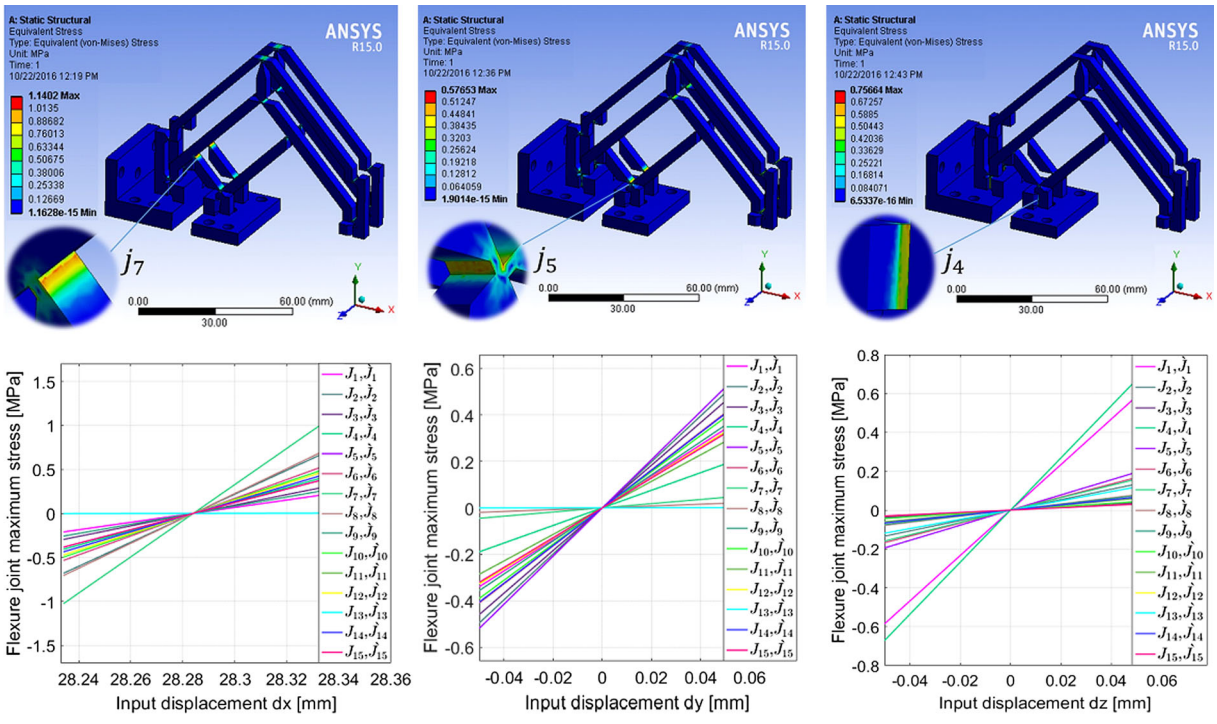

(a) Motion in x-axis (b) Motion in y-axis (c) Motion in z-axis

Fig. 24 Maximum Stress of the flexure joints versus input displacements d_x, d_y and d_z

9 Conclusions

A novel 3D compliant manipulator utilizing flexure joints is designed based on parallelogram linkage for micromanipulation. The manipulator has 3 translational DOF in the three orthogonal axes x, y and z and uses three linear actuators. The results of the kinematic analysis show a decoupled translation motions with a fixed orientation of the end-effector. The singularity-free-workspace is derived in closed form taking into account the physical limits of flexure joints. The usable workspace is determined as the maximum cuboid inscribed inside the reachable workspace. The dexterity analysis is also carried out. A synthesis methodology of the proposed manipulator is developed. The main contribution of this study is that the ratio of the entire workspace volume to installation volume of the proposed manipulator is very high compared with aforementioned manipulators. Moreover, the linear actuators can be placed in such a way to act at the same point in order to achieve isotropic performance over the whole workspace. The proposed manipulator can be used to give identical, enlarged or miniaturized motion with respect to the actuators' displacements. The trade-off between resolution and workspace volume determines the suitable manipulator design for many micro/nano-applications to deal with the limited stroke variety of PZT actuators. The translational decoupling with small 5 DOF parasitic motions have been experimentally verified. The linearity between input and output displacements have been also confirmed using finite element method and experimental tests.

Acknowledgment The first author is supported by a scholarship from the Mission Department, Ministry of Higher Education of the Government of Egypt which is gratefully acknowledged.

References

1. Li, Y., Xu, Q.: Design and optimization of an xyz parallel micromanipulator with flexure hinges. J. Intell. Robot. Syst. **55**(4-5), 377–402 (2009)
2. Tan, F., Sun, L., Rong, W., Zhu, J., Xu, L.: Modeling of micromanipulation robot in virtual environment. Acta Metallurgica Sinica-English Letters- **17**(2), 194–198 (2004)

3. Hammond, F.L., Howe, R.D., Wood, R.J.: Dexterous high-precision robotic wrist for micromanipulation. In: 2013 16th International Conference on Advanced Robotics (ICAR), pp. 1–8. IEEE (2013)
4. Wang, J., Gosselin, C.M.: A new approach for the dynamic analysis of parallel manipulators. Multibody Sys.Dyn. **2**(3), 317–334 (1998)
5. Hao, F., Merlet, J.-P.: Multi-criteria optimal design of parallel manipulators based on interval analysis. Mech. Mach. Theory **40**(2), 157–171 (2005)
6. Zettl, B., Szyszkowski, W., Zhang, W.: Accurate low dof modeling of a planar compliant mechanism with flexure hinges: the equivalent beam methodology. Precis. Eng. **29**(2), 237–245 (2005)
7. Smith, S.T.: Flexures: elements of elastic mechanisms. CRC Press (2000)
8. Tian, Y., Shirinzadeh, B., Zhang, D., Zhong, Y.: Three flexure hinges for compliant mechanism designs based on dimensionless graph analysis. Precis. Eng. **34**(1), 92–100 (2010)
9. Ma, H.-W., Yao, S.-M., Wang, L.-Q., Zhong, Z.: Analysis of the displacement amplification ratio of bridge-type flexure hinge. Sensors Actuators A Phys. **132**(2), 730–736 (2006)
10. Liaw, H.C., Shirinzadeh, B.: Robust generalised impedance control of piezo-actuated flexure-based four-bar mechanisms for micro/nano manipulation. Sensors and Actuators A Phys. **148**(2), 443–453 (2008)
11. Zhang, D., Chetwynd, D.G., Liu, X., Tian, Y.: Investigation of a 3-dof micro-positioning table for surface grinding. Int. J. Mech. Sci. **48**(12), 1401–1408 (2006)
12. Zhang, A., Chen, G.: A comprehensive elliptic integral solution to the large deflection problems of thin beams in compliant mechanisms. J. Mech. Robot. **5**(2), 021006 (2013)
13. Lyon, S.M., Howell, L.L.: A simplified pseudo-rigid-body model for fixed-fixed flexible segments. In: ASME 2002 International Design Engineering Technical Conferences and Computers and Information in Engineering Conference, pp. 23–33, American Society of Mechanical Engineers (2002)
14. Kimball, C., Tsai, L.-W.: Modeling of flexural beams subjected to arbitrary end loads. J. Mech. Des. **124**(2), 223–235 (2002)
15. Boyle, C.: A closed-form dynamic model of the compliant constant-force mechanism using the pseudo-rigid-body model (2003)
16. Howell, L.L., Magleby, S.P., Olsen, B.M.: Handbook of compliant mechanisms. Wiley (2013)
17. Kang, B.H., Wen, J.T.-Y., Dagalakis, N., Gorman, J.J.: Analysis and design of parallel mechanisms with flexure joints. IEEE Trans. Robot. **21**(6), 1179–1185 (2005)
18. GuÃŚrinot, A.E., Magleby, S.P., Howell, L.L., Todd, R.H.: Compliant joint design principles for high compressive load situations. J. Mech. Des. **127**(4), 774–781 (2005)
19. Horie, M., Kamiya, D., Uchida, T., Urata, M., Ikegami, K.: New miniature pantograph mechanisms with large-deflective hinges for micro-bonding by adhesives. In: International Symposium on Electronic Materials and Packaging, 2000. (EMAP 2000), pp. 167–174, IEEE (2000)
20. Ishii, Y., Thümmel, T., Horie, M.: Dynamic characteristic of miniature molding pantograph mechanisms for surface mount systems. Microsyst. Technol. **11**(8-10), 991–996 (2005)
21. Gosselin, C.M., Masouleh, M.T., Duchaine, V., Richard, P.-L., Foucault, S., Kong, X.: Parallel mechanisms of the multipteron family: kinematic architectures and benchmarking. In: 2007 IEEE International Conference on Robotics and Automation, pp. 555–560, IEEE (2007)
22. Li, Y., Xu, Q.: Kinematic analysis and design of a new 3-dof translational parallel manipulator. J. Mech. Des. **128**(4), 729–737 (2006)
23. Yoshikawa, T.: Manipulability and redundancy control of robotic mechanisms. In: 1985 IEEE International Conference on Robotics and Automation. Proceedings., vol. 2, pp. 1004–1009, IEEE (1985)
24. Li, Y., Xu, Q.: Kinematic design of a novel 3-dof compliant parallel manipulator for nanomanipulation (2005)

Abdullah T. Elgammal was born in Alexandria, Egypt, in 1988. He has received the B.Sc. in control and measurements from Benha University, Kalyobiya, Egypt and received the M.Sc. degree in mechatronics and robotics from Egypt-Japan University of Science and Technology (EJUST), Alexandria, Egypt. He is currently working toward the Ph.D. degree in mechatronics and robotics at EJUST. His research interests include micromanipulation, robot design, robust control, robot kinematics, dynamic and modeling.

Mohamed Fanni received the B.E. and M.Sc. degrees in mechanical engineering from Faculty of Engineering of both Cairo University and Mansoura University, Egypt, in 1981 and 1986, respectively and the Ph.D. degree in engineering from Karlsruhe University, Germany, 1993. He is an Associate Professor with Innovation, Graduate School of Engineering Science, Egypt-Japan University of Science and Technology E-JUST, Alexandria, on leave from Production Engineering & Mechanical Design Department, Faculty of Engineering, Mansoura University, Egypt. His major research interests include robotics engineering, automatic control, and Mechanical Design. His current research focuses on Design & Control of Mechatronic Systems, Surgical Manipulators, Teleoperation systems and Flying/Walking Robots.

Abdelfatah M. Mohamed has received the Ph.D degree from University of Maryland, College park, USA in 1990. Since 1990 he has been an Assistant Professor with the Dept. of Electrical Engineering, Assiut University, Egypt. He became an Associate Professor in 1995, and Professor in 2000. From September 1990 to August 1993, He has been a Postdoctoral Fellow at the Dept. of Mechanical Engineering, University of Texas, Austin USA. From April 1996 to April 1997, He has been a visiting Professor at the Dept. of Electrical Engineering, Kanazawa University, Japan. From September 2010 to March 2012 He has been the Head, Dept. of Electrical Engineering, Assiut University, and became the Dean of Faculty of Engineering, Assiut University on March 2012. Currently He is a professor at the Dept. of Mechatronics and Robotics Engineering, Egypt-Japan University of Science & Technology. His research interest lies in Robust and Intelligent control, Magnetic Bearing systems, Robotics, Industrial drives. Dr. Mohamed is a senior IEEE member.